Radiation Physics and Engineering 2025; ?(?):?-?

### Impact of polymer shielding layer on absorbed dose distribution in an 18 MeV LINAC treatment room: A FLUKA simulation study

Eskandar Asadi Amirabadi<sup>a,\*</sup>, Mohammad Reza Pahlavani<sup>a</sup>, Nima Ghal-Eh<sup>b</sup>

- <sup>a</sup> Department of Nuclear Physics, Faculty of Basic Science, University of Mazandaran, P.O. Box 47415-416, Babolsar, Iran
- <sup>b</sup>Department of Physics, Faculty of Science, Ferdowsi University of Mashhad, P.O. Box 91775-1436, Mashhad, Iran

#### HIGHLIGHTS

- A C/D2300 linac head manufactured by Varian were simulated within a radiation therapy room.
- An alternative photon source was utilized, instead of starting all the calculations from the primary electron beam.
- Designing of a multilayer shield for the walls of treatment rooms, as the interior covering of the treatment room.
- Using a polymer shielding layer effect significantly on reducing photon and neutron absorbed dose.

#### ABSTRACT

In this study, using the FLUKA code (version 2011.2c.6), a C/D2300 linear accelerator head manufactured by Varian (18 MeV) were simulated within a radiation therapy room. Electron source and transporting particles using the FLUKA code from the source in each calculation replaced by an alternative photon which is an important aspect of the work. After verifying this alternative source, a composite shielding layer was considered as the interior covering of the treatment room, and the effect of six polymer-based shielding materials with different compositions on the photon and neutron doses at different locations was calculated. As a general conclusion from this research, using a polymer shielding layer of material including 32.5 wt% elastomer +60 wt% tungsten +7.5 wt% boron carbide on the interior of the roof, floor, and concrete walls of the treatment room is recommended, except for the second wall at the maze entrance. Additionally, we found that a 2 cm thickness of this shield is almost equivalent to 3 mm of pure lead. The optimized thickness depends on the specifications of the LINAC, its energy, the dimensions of the treatment room, and the thickness of the concrete walls which can be calculated based on these specifications.

#### KEYWORDS

Medical Linear Accelerator Shielding FLUKA

FLUKA

Absorbed Dose

Photon

Neutron

#### HISTORY

Received:

Revised:

Accepted:

Published:

#### 1 Introduction

Linear accelerators (LINACs) are widely employed in the field of oncology for cancer treatment, primarily by generating electron beams that subsequently produce high-energy X-rays for beam therapy. Superficial tumors are typically treated using the electron mode of the LINAC, while deep-seated tumors require high-energy X-rays generated in photon mode (Funk et al., 2016). When a LINAC operates with primary beam energy exceeding 8 megavolts (MV) in photon mode, the interaction of high-energy photons with materials of high atomic number (Z) - such as the LINAC head, collimators, treatment room components, and even the patient - can result in the undesirable generation of neutrons through bremsstrahlung radiation. This phenomenon, referred to as neutron contamina-

tion, results in the concurrent production of photons, neutrons, and electrons of varying energies within the treatment room. Although electrons possess limited penetration depth and can be disregarded for shielding considerations, effective shielding against photons and neutrons is crucial to mitigate radiation exposure for patients, health-care personnel, and the general public (Hassan et al., 2018; Horst et al., 2015; Soppera et al., 2017; Vega-Carrillo et al., 2012; Howell et al., 2009).

The walls of the treatment room are subjected to two distinct types of radiation: primary beams and scattered or leakage radiation. Typically, the walls that are directly exposed to primary radiation are significantly thicker than those that only encounter scattered and leakage radiation. In their study, Hernndez et al. (Hernandez-Adame et al.,

<sup>\*</sup>Corresponding author: e.asadi@umail.umz.ac.ir

2011) examined the optimized thickness of various treatment room walls, referencing the guidelines set forth by the National Council on Radiation Protection and Measurements in Report 151.

To design an effective homogeneous shield for a radiotherapy treatment room, concrete with varying densities is the predominant material choice, owing to its costeffectiveness, environmental compatibility, ease of construction, minimal maintenance requirements, and favorable mechanical properties. To enhance the attenuation characteristics of concrete, the incorporation of high atomic number elements or their compounds as fillers has proven beneficial. Recent studies have demonstrated that the addition of micro- or nano-particle fillers, such as bismuth oxide (Bi<sub>2</sub>O<sub>3</sub>) (El-Nahal et al., 2021), tungsten oxide (WO<sub>3</sub>) (Tekin et al., 2017), and lead oxide (PbO) (Verdipoor and Mesbahi, 2020), not only reduces porosity and modifies the structural composition of concrete but also increases its density. These modifications result in significant improvements in critical parameters, such as the mass attenuation coefficient, thereby enhancing the material's effectiveness as a radiation shield (Rosenberg, 2008; Ashoor et al., 2019).

An alternative approach to shielding design involves the use of multiple layers of materials, where shields are arranged sequentially, one behind the other (Wille, 2000). Numerous studies have demonstrated that high-density, flexible, and lightweight polymer matrices infused with filler particles can significantly enhance shielding properties (Ali et al., 2018; Salimi et al., 2018; Soltani et al., 2016; Asgari et al., 2021). However, the feasibility of using these polymer shields in isolation - specifically, as a replacement for concrete in LINAC rooms - necessitates a more comprehensive investigation. In contrast, the potential benefits of implementing a multilayer shielding strategy, which incorporates a polymer layer in conjunction with a concrete base for LINAC rooms, represents a promising area of research that warrants further exploration.

The primary objective of this research is to evaluate the efficacy of a polymer-based shielding layer designed to maximize the attenuation of photon and neutron leakage from treatment rooms, thereby ensuring radiation protection for staff, patient companions, and visitors. The polymer shield is strategically implemented as a distinct layer over a concrete substrate within the room.

Our purpose in investigating this polymer-based shield is to use it in the LINAC room without destruction. We want to show this type of shielding is capable of adding to the concrete wall of the treatment room when the equipment of the room becomes upgraded, and also, it can also be used in places where space is limited and reduces the required concrete thickness. This shield is composed of an elastomeric material formulated from a blend of chloroprene rubber and natural rubber (CR&NR), which is enhanced with high-capacity fillers specifically engineered to absorb both photons and neutrons.

In radiation detection and dosimetry, particularly concerning neutrons, studies conducted in actual accelerator treatment rooms are often accompanied by the inherent risk of radiation exposure. To mitigate these risks, Monte Carlo simulations serve as a valuable virtual laboratory for such investigations. This study employs the Monte Carlo code FLUKA (FLUktuierende KAskade) (Ferrari et al., 2005) to perform these simulations.

#### 2 Materials and methods

Monte Carlo (MC) simulations have emerged as a robust tool in radiotherapy, facilitating comprehensive analyses of the performance of individual components within LINAC heads. These simulations offer critical insights into beam characteristics, radiation fields, and dosimetry parameters, enhancing our understanding of treatment delivery and optimization (Jabbari and Hashemi-Malayeri, 2009). This study was performed using the FLUKA code (version 2011.2c.6). This code is renowned for its ability to accurately simulate the interactions and transport of approximately 60 different particle types, including photons and electrons across a wide energy range from 100 eV to several TeVs, hadrons with energies up to 20 TeV, as well as all antiparticles. Furthermore, FLUKA is capable of modeling neutrons down to thermal energies and heavy ions. An advanced user interface, known as Flair, enhances the usability of the FLUKA code, facilitating a more intuitive interaction with the simulation environment (Ferrari et al., 2005).

#### 2.1 Geometry

In this work, using FLUKA code, different components of a C/D2300 linear accelerator head manufactured by Varian (18 MeV) were simplified and simulated in actual sizes within a radiation therapy room. This simplification has been employed in many studies involving the simulation of medical linear accelerators (Howell et al., 2009; Abdul Haneefa et al., 2014; Martinez-Ovalle et al., 2011; Dawn et al., 2018). The main components of the LINAC head include the target, composed of tungsten and copper, the flattening filter, made of iron and tantalum, and the primary and secondary collimators (i.e., jaws) made of tungsten. The simulated geometry is illustrated in Fig. 1.

The target system comprises two distinct layers: an upper tungsten cylinder and a lower copper cylinder. The tungsten layer, which serves as the primary target for bremsstrahlung X-ray photon production, has a radius of 0.3 cm and a height of 0.06 cm. Directly underneath and attached to the tungsten layer is the copper cylinder, which also has a radius of 0.3 cm but a height of 1 cm. The interaction between the high-energy electrons and the tungsten layer results in a significant conversion of kinetic energy into heat, leading to an increase in temperature that can adversely affect the material properties of tungsten. To mitigate oxidation and prevent degradation of the tungsten layer, it is crucial to maintain its temperature below 351 K. Additionally, the copper layer plays a vital role in the system by absorbing low-energy photons that do not contribute to the treatment. This absorption process helps to reduce the photon flux in the vicinity of the patient, thereby enhancing the overall safety and effectiveness of the treatment (Auditore et al., 2005; Wang et al., 2017).

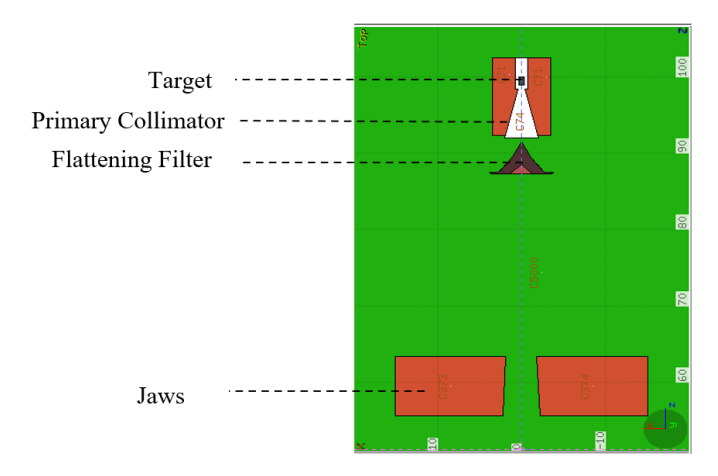
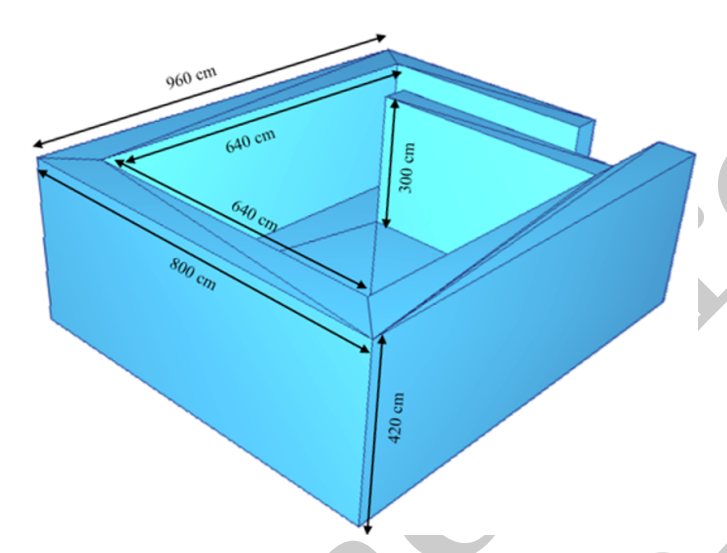


Figure 1: Geometry of the medical linear accelerator head simulated with the FLUKA code (dimensions are in cm).



**Figure 2:** A 3D view of the LINAC room and internal and external dimensions.

In the next simulation step, the treatment room was considered with external dimensions of  $420\times800\times960~\mathrm{cm^3}$ . The internal dimensions of the room are  $300\times640\times640~\mathrm{cm^3}$ . The treatment room and its dimensions are shown in a 3D view in Fig. 2. The walls and floor of the room were constructed of concrete (with a density of  $2.35~\mathrm{g.cm^{-3}}$ ) featuring a wall thickness of 80 cm and a ceiling thickness of 40 cm. The middle wall in the maze was also made of concrete with a thickness of 60 cm. The selected wall thicknesses for the simulations were based on the dimensions of a real treatment facility. It is noteworthy that the tenth value layer (TVL) for high-energy X-rays, specifically in the range of 10 to 25 MeV, is estimated to be between 40 and 50 cm in concrete (Morgan et al., 2006).

The programs were run on a computer equipped with an Intel Core i9-7900 processor, operating at  $3.30~\mathrm{GHz}$ , and featuring  $32~\mathrm{GB}$  of RAM.

#### 2.2 Alternative photon source

In line with the objectives of this research, the calculations need to be performed from the electron beam to the walls of the treatment room, which is very time-consuming and involves transporting billions of electrons.

In many studies conducted in the field of medical linear accelerators using the MCNP code, the SSW card was employed to save particle information on a surface as a source (to generate phase space), and the SSR card is used to read this information in subsequent calculation steps that it reduces program execution time and also, minimize uncertainty in the calculations (McConn et al., 2011; Abella et al., 2010; Toossi et al., 2013). Inspired by this capability in the MCNP code, as an innovation in the present study, instead of using an electron source and transporting particles started from the source in each calculation in the FLUKA code, an alternative photon source (with an energy spectrum dependent on the emission direction, exhibiting similar behavior to an integrated simulation) was utilized in the calculations.

Therefore, to optimize execution time and minimize uncertainty in the calculations, the program execution was divided into two distinct stages:

- 1) Definition of the electron source: The electron source was characterized as a thin pencil beam with a radius of 0.05 cm and an energy of 18 MeV. This source is positioned anterior to and elevated above the target, utilizing the BEAM and BEAMPOS cards of the FLUKA code. The electron beam is directed perpendicularly toward the target, which facilitates the emission of bremsstrahlung X-rays from the target surface. The distance from the electron source to the isocenter was set at 100 cm.
- 2) Generation of phase space around the target: High energy electrons interact with the target (as a material with a high atomic number) via the bremsstrahlung radiation and then, photons are emitted from the target and scattered in its vicinity. We recorded the information of these photons (i.e., phase-space). To characterize the phase space surrounding the target, we defined a spherical region centered on the target itself. We then calculated both the energy and angular distributions of bremsstrahlung X-ray photons emitted from the target's surface within this spherical volume. The energy distribution was obtained using the USRBDX, while the angular distribution was derived from the USRYIELD cards, respectively. The USRBDX card functions as a boundarycrossing estimator, providing double differential distributions of fluence or current as a function of energy for particles crossing the boundaries of the sphere. In contrast, the USRYIELD card quantifies the double differential particle yield in the vicinity of either a point or extended target.
- 3) Definition of an alternative photon source: An alternative photon source uses the phase space information-specifically, the energy and angular distribution of photons-surrounding the target for subsequent calculations. In this approach, calculations are conducted once, from the electron beam to the vicinity of the target, after which all subsequent analyses are initiated from the emission of photons within a defined sphere around the target. Conventional source definition cards, such as BEAM and BEAMPOS, do not allow for the specification of a source characterized by a unique energy spectrum and angular distribution. To address this limitation, one has to im-

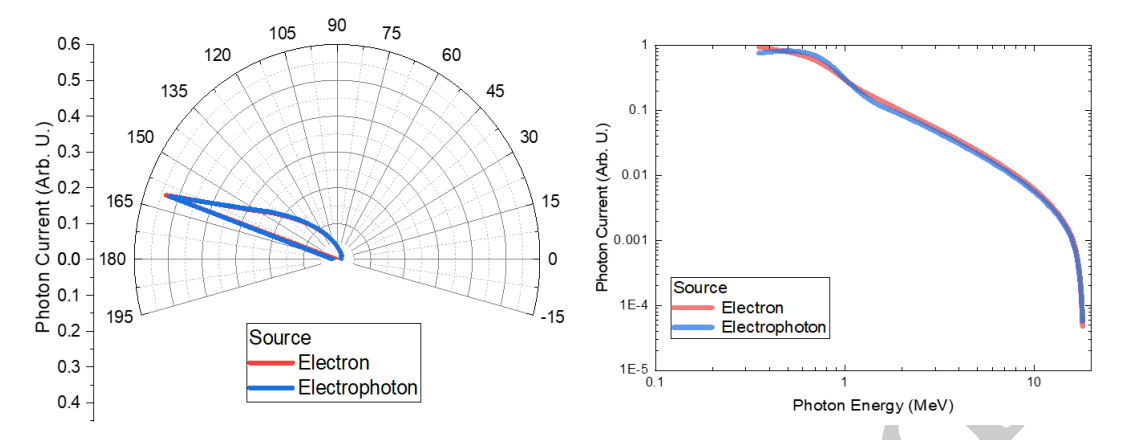


Figure 3: Comparison of the energy spectrum and angular distribution of photons emitted from the electron source and the alternative photon source simulated by FLUKA.

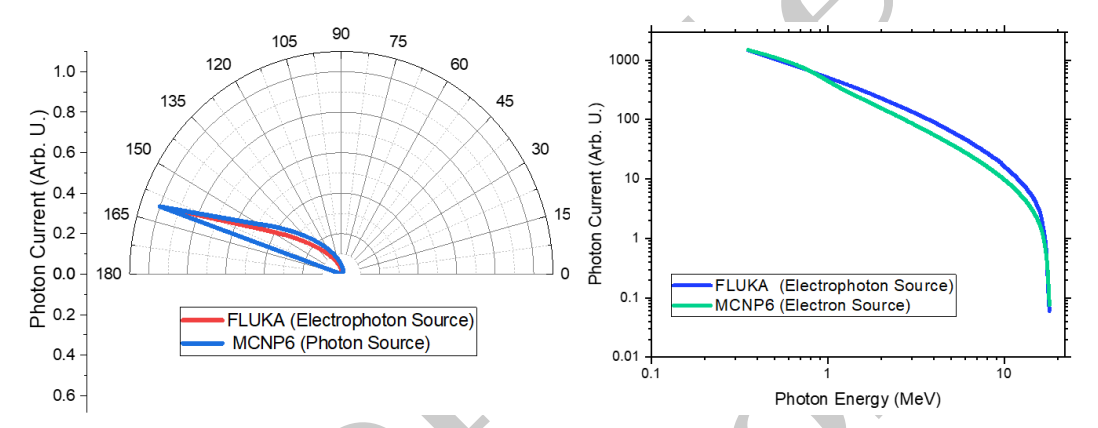


Figure 4: Comparison of the energy spectrum and angular distribution of photons emitted from the electron source (simulated by MCNP6 code) and the alternative photon source (simulated by FLUKA code).

plement Fortran user routines within the FLUKA code (source.f) to construct the necessary input file.

#### 2.3 Verification of the alternative photon source

# 2.3.1 Energy spectrum and angular distribution of Bremsstrahlung X-rays photons simulated by FLUKA

To ensure the accuracy of the calculations involving the alternative photon source, we compared the energy and angular distribution of photons generated by the 18 MeV electron source - using the USRBDX and USRYIELD cards - on the surface of the sphere surrounding the target with the results from the proposed photon source, as illustrated in Fig. 3.

The comparison reveals a promising agreement between the results obtained from both sources. To verify the subsequent calculations, the energy spectrum and angular distribution of photons from the electron source and the alternative photon source were compared. Figure 3 shows a comparison of the results obtained from the electron source with an energy of 18 MeV (using USRBDX and USRYIELD cards) on the surface of the sphere surrounding the target with the results of the proposed photon source. A remarkable agreement is observed between the results obtained from these two sources.

# 2.3.2 Energy spectrum and angular distribution of Bremsstrahlung X-rays of the electron source simulated by MCNP6 and the alternative photon source simulated by FLUKA

Initially, we simulated the same geometry using the Monte Carlo code MCNP6, version 6.1 (Goorley et al., 2012). Subsequently, we compared the energy spectrum and angular distribution of photons around the target, as obtained from the alternative photon source using the FLUKA code, with the results derived from an electron source in MCNP6. This comparison was conducted to verify the findings associated with the alternative photon source. The results of this comparison are depicted in Fig. 4, which demonstrates a strong correlation between the results calculated by both Monte Carlo codes concerning the energy and angular distribution of X-photons around the target.

Overall, the findings illustrated in Figs. 3 and 4 indicate that the peak intensities of X-photons are closely aligned across the two methodologies. Specifically, for an 18 MeV electron beam, the maximum photon current (peak photon intensity) is observed at approximately 0.5 MeV. Furthermore, it is evident that for any primary electron beam (e.g., 18 MeV), the maximum energy of the bremsstrahlung X-ray photons corresponds to the energy of the incident electrons, which in this instance is 18 MeV.

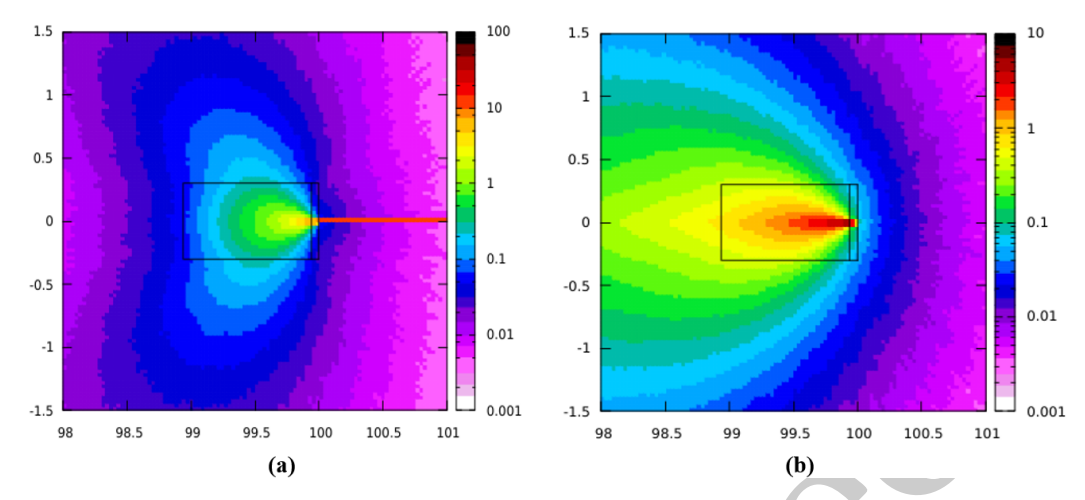


Figure 5: a) Distribution of electron fluence resulting from the impact of an electron beam on the target., b) Distribution of bremsstrahlung X-ray photons inside and around the target (Units are in cm).

Additionally, Figs. 3 and 4 show a comparison of the angular distribution of X-ray photons produced around the target as calculated by the FLUKA code using the USERYIELD card and by the MCNP6 code utilizing the F1 tally and the C1 card (for angular segmentation) and also the FT1 card with the FRV parameter (for determining the desired reference direction in angular segmentation). Notably, the amount of photon current in each angular interval is shown on the first value of that interval. The maximum current of photons falls within the angle 160.50 which corresponds to the angular interval 160.50 to 180°, the area directed towards the patient and its surroundings. The angle of 180 is oriented directly towards the patient.

#### 2.4 Shielding calculations

The mixed photon and neutron fields generated by medical linear accelerators in treatment rooms necessitate a thorough assessment of photon and neutron doses in the surrounding walls, floor, and ceiling. To facilitate this evaluation, ICRU spheres were strategically positioned at various locations both inside and outside the treatment room to measure the absorbed doses. These measurements serve as a basis for calculating the absorbed dose in these regions. Subsequently, a composite shielding layer was implemented as the interior lining of the treatment room, and the impact of this shielding on photon and neutron doses was analyzed. This study explored six polymerbased shielding materials with varying compositions, assessing their effectiveness in reducing radiation exposure around the isocenter, as well as behind the walls, above the ceiling, and beneath the floor of the treatment room.

#### 3 Results and discussion

# 3.1 2D distribution of electron beam and bremsstrahlung photons emitted from the target

In the FLUKA code, the USRBIN card scores various quantities, such as energy deposition density, dose, and

particle fluence, across a regular spatial grid (rectangular, cylindrical, or spherical) that is independent of the underlying geometry. We utilize the USRBIN feature to illustrate the two-dimensional distribution of particle fluence, as depicted in Fig. 4.

Figure 4-a shows the electron beam (18 MeV) and the corresponding distribution of electron fluence around the target. It is evident that upon impact with the target, the electrons undergo substantial energy loss, primarily attributed to bremsstrahlung radiation. Following this initial loss, the electrons continue to dissipate their remaining energy through collisions with atomic electrons, ultimately coming to rest after traversing only a short distance. This decrease in energy is visually represented by the transition of colors in the affected regions, shifting from red to purple.

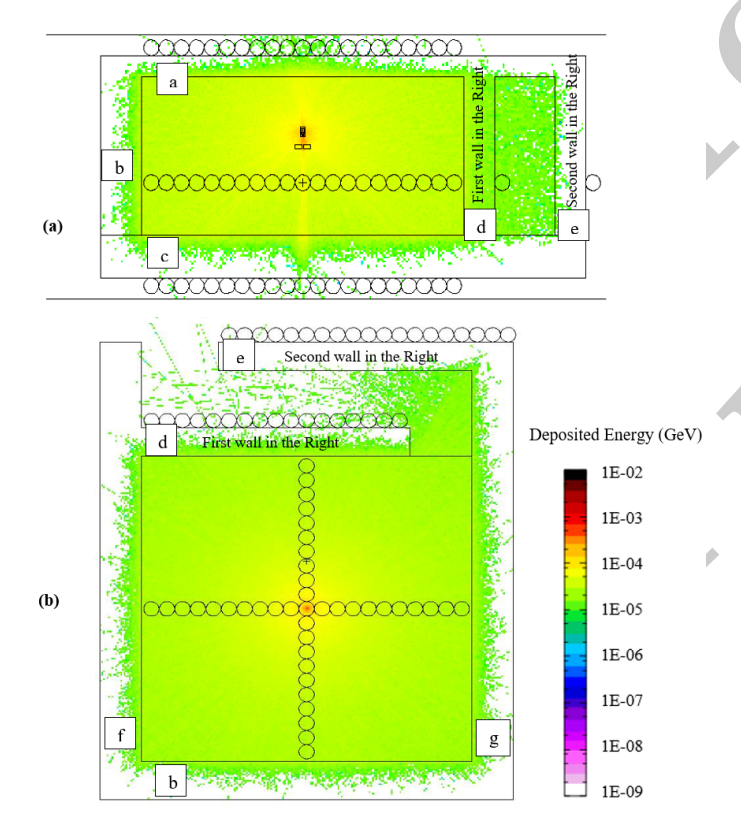
Figure 5-b displays the distribution of bremsstrahlung X-ray photons generated from the interactions of the electron beam with the target. Notably, the intensity of the bremsstrahlung X-ray photons produced within the tungsten layer is predominantly aligned with the direction of the primary electron beam. Furthermore, the energy of these photons is several orders of magnitude greater than that of the incident electrons, highlighting the efficiency of the bremsstrahlung process in converting kinetic energy into high-energy X-ray photons.

#### 3.2 Distribution of photon and neutron deposition energies inside and outside the treatment room

The head shielding of a LINAC is essential for reducing radiation exposure to the patient; however, it has limitations in effectively controlling photoneutrons. Moreover, photonuclear reactions  $(\gamma, n)$  occurring within the heavy metal components of the head may inadvertently increase the production of photoneutrons. Typically, the head shielding is composed of materials such as tungsten, lead, and iron, with variations in thickness, shape, and composition depending on the specific type of accelerator and its operational energy levels (Horst et al., 2015;

Patil et al., 2011; Brkić et al., 2018). Due to the complexities involved and the unavailability in obtaining accurate details regarding these parameters (Horst et al., 2015), many simulations of the LINAC head simplify the model by omitting this shielding (Edwards and Mountford, 2004; Ma et al., 2008; McConn et al., 2011). Consequently, the present study also excludes consideration of the head shielding.

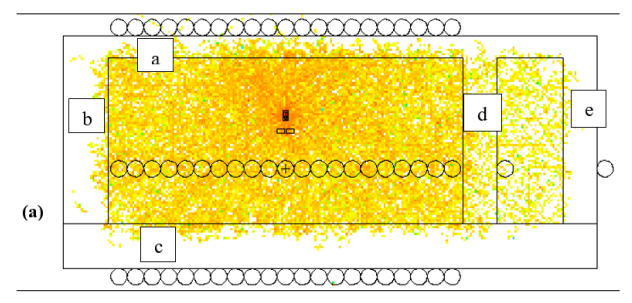
As previously mentioned, medical linear accelerators generate mixed photon and neutron fields during treatment, necessitating an assessment of the photon and neutron doses in the walls of the treatment room. To facilitate this, ICRU spheres were strategically placed at various locations both inside and outside the treatment room to measure absorbed doses. The energy deposition densities for photons and neutrons were calculated using the US-RBIN calculator, with the results depicted in Figs. 6 and 7, respectively. In these figures, a transition in heat map colors from red to green signifies a decrease in the deposited energy of the particles. For clarity, the walls are designated with lowercase letters.



**Figure 6:** Distribution of photon deposition energy within the treatment room and its penetration into the walls, presented in two perspectives: a) y-z view and b) x-y view. The color bar indicates energy values in giga-electronvolts (GeV).

**Table 1:** Weight percentages of different components of concrete (McConn et al., 2011).

Element	ZAID $(1000 \times Z + A)$	Weight Fraction
С	6012	0.000124
N	7014	0.745268
O	8016	0.231781
$\operatorname{Ar}$	18038	0.012827



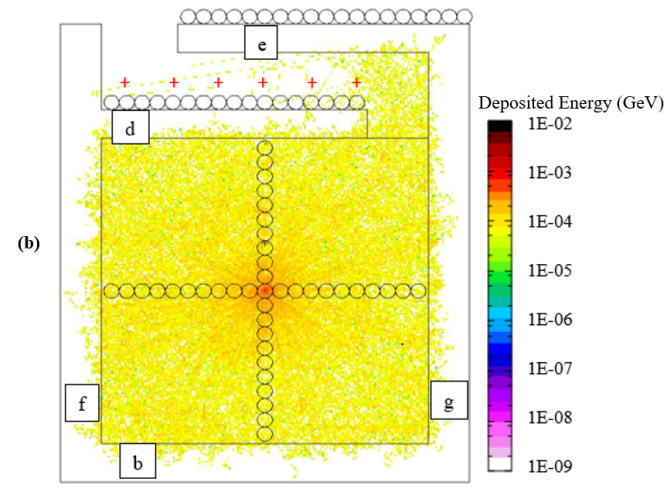


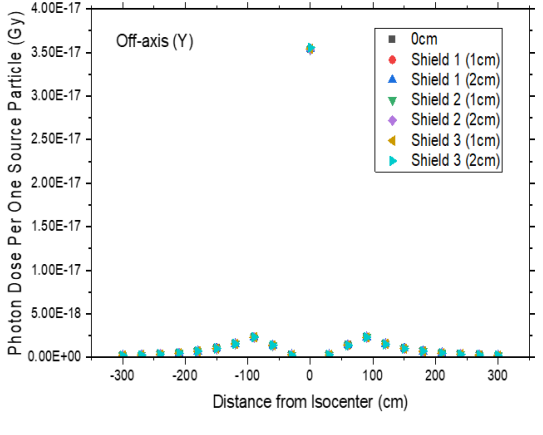
Figure 7: Distribution of neutron deposition energy within the treatment room, highlighting its penetration into the surrounding walls. The data is illustrated from two perspectives: a) the y-z view and b) the x-y view. Energy values indicated in the color bar are in GeV.

In Figure 6-a, it is evident that the intensity of the photon field is heightened along the treatment beam, particularly at the ceiling (a) and the floor (c) of the room. Photons striking wall (b) appear to be nearly fully absorbed, while significant leakage is observed from the middle wall of the maze, especially at the door. Figure 6(b) illustrates the arrangement of ICRU spheres in a "+" configuration along the x and y axes (perpendicular to the beam), all aligned at the same height as the isocenter. The central sphere, located at the intersection of the x and y axes, is positioned at the isocenter, where the radiation beams converge during gantry rotation. The isocenter is a critical reference point in the LINAC treatment room and serves as the calibration point for the irradiation field size. In this study, as in many others, the isocenter is defined as the origin of the coordinate system. Figure 7 illustrates the schematic of photoneutron contamination in the LINAC room.

In contrast to photon distributions, neutron fluence demonstrates a relatively uniform profile throughout the treatment area, with notable exceptions in proximity to the head and the isocenter. This observation indicates that photoneutron contamination is broadly distributed across the treatment room. Although neutrons can penetrate the middle wall of the maze, the reduced density of neutron spots observed in the corridor signifies a substantial decrease in neutron energy deposition. It is evident that neutrons are predominantly absorbed by both the wall (b) and the floor (c) of the room. However, due to

Number	Name	Density $(g.cm^{-3})$	Elastomer%	Lead%	Tungsten%	Boron Carbide%
1	Shield 1	1.48	62.5	30	0	7.5
2	Shield 2	1.86	47.5	45	0	7.5
3	Shield 3	2.47	32.5	60	0	7.5
4	Shield 4	1.50	62.5	0	30	7.5
5	Shield 5	1.91	47.5	0	45	7.5
6	Shield 6	2.61	32.5	0	60	7.5

Table 2: Weight percentages of different components of polymeric shielding materials.



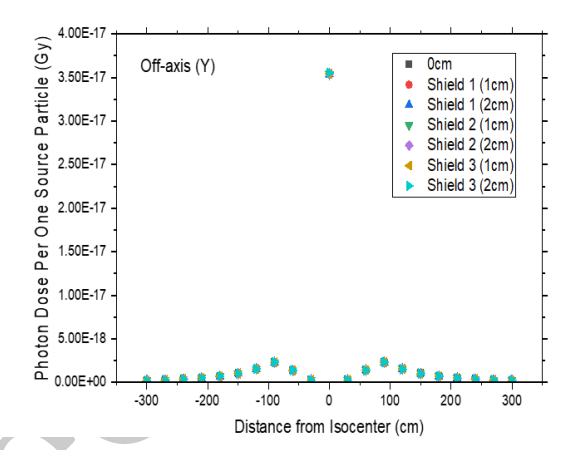


Figure 8: Photon dose along the two axes perpendicular to the treatment beam (x and y directions) with and without the shielding layer of Shield 1, Shield 2, and Shield 3 materials.

the positioning of the primary beam and head components closer to the ceiling, neutrons can penetrate more significantly into the ceiling (a), and in some cases, may even traverse through it.

# 3.3 Photon absorbed dose in different locations inside treatment room with and without polymer shielding

The walls of the radiotherapy room are normally made of ordinary concrete (with a density of 2.35 g.cm<sup>-3</sup>). Elemental compositions and the related weighting percentages of concrete are given in Table 1 (McConn et al., 2011).

In previous studies, to create a homogeneous shielding layer, the effect of different concrete compositions of walls on the equivalent dose (Razghandi et al., 2021), the effect of adding photon- and neutron-absorbing nanoparticles to concrete (Tekin et al., 2017; Verdipoor and Mesbahi, 2020; Ghasemi-Jangjoo and Ghiasi, 2019), and the optimal percentage of boron carbide in the mixed gammaneutron fields (Salimi et al., 2018; Soltani et al., 2016; Asgari et al., 2021) have been investigated. However, in this study, a polymer shielding layer was added to the interior of the concrete walls, floor, and ceiling of the radiotherapy room and it resulted multilayer shield.

The concept of using a multilayer shield in radiation therapy rooms has been explored in previous studies. Kosako et al., (Kosako et al., 2014) aiming to design an optimal shielding solution for the walls of a medical linear accelerator facility, investigated a multilayer shield composed of iron, polyethylene, lead, and concrete with varying thicknesses. They ultimately determined the optimal arrangement of this shield with a total thickness of 100 cm, structured as 40 cm of iron, 10 cm of polyethy-

lene, 20 cm of iron, 10 cm of lead, 10 cm of polyethylene, and 10 cm of concrete. In another study, Uddin et al. examined the strategic aspects of the shielding in a LINAC room. They proposed a multilayer shield consisting of a layer of high atomic number materials (such as lead, tungsten, steel, etc.) placed between the two layers of concrete (Uddin et al., 2024).

The polymer shielding materials consist of an elastomeric material (based on chloroprene rubber and natural rubber (CR&NR) with high fillability, containing photonand neutron-absorbing fillers. The specifications of six shielding materials studied in this work are listed in Table 2. The percentages of the components are chosen according to the results of our previous studies fields (Salimi et al., 2018; Soltani et al., 2016; Asgari et al., 2021).

The photon absorbed dose was calculated at various locations: on the outer surfaces of the walls, above the ceiling, and beneath the floor of the room, both with and without the incorporation of the polymeric shield. Subsequently, the results obtained from six different shielding materials evaluated at two different thicknesses were compared. These calculations were performed using ICRU spheres, according to the geometry depicted in Figs. 6 and 7. The radiation field dimensions were set to 10 cm  $\times$  10 cm. The simulations were run for 5E8 histories, yielding a relative error of less than 1% in the photon dose calculations.

First, the photon absorbed dose along the two axes perpendicular to the treatment beam (x and y directions) was investigated. As illustrated in Fig. 8, the photon dose reaches its maximum value at the isocenter where the treatment area is centered. The photon dose value decreases suddenly in the vicinity of the isocenter. Notably,

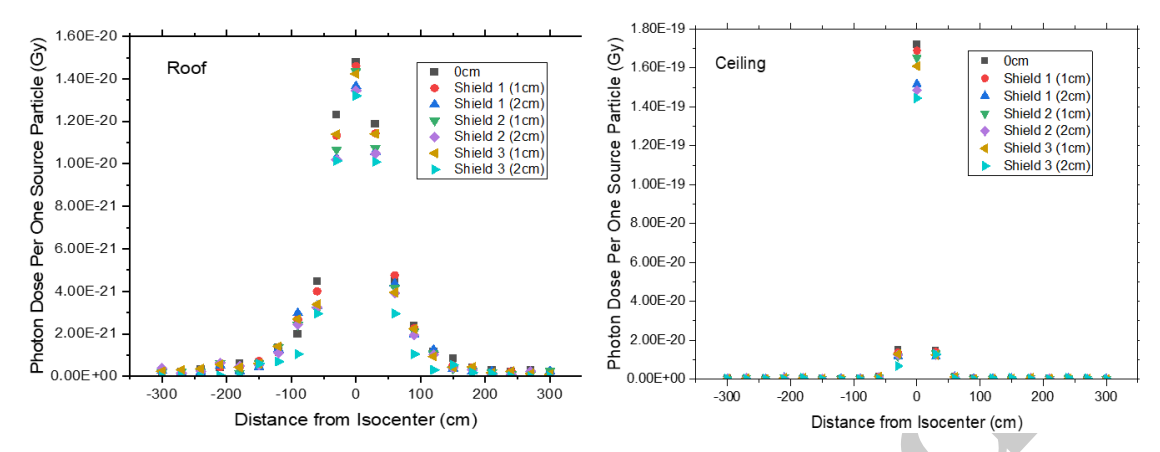


Figure 9: Photon absorbed dose (a) above the ceiling and (b) below the floor of the treatment room, with and without the shielding layer of Shield 1, Shield 2, and Shield 3 materials.

adding a polymer shielding layer to the concrete walls of the treatment room does not significantly impact the reduction of photon dose in a plane perpendicular to the treatment beam, centered at the isocenter.

Second, we assessed the photon dose in regions above the ceiling and below the floor, with results illustrated in Fig. 9. In the simulations, the concrete thickness of the ceiling (40 cm) was assumed thinner than the thickness of the floor (80 cm). This difference is due to the orientation of the treatment beam, which is directed toward the floor, necessitating a more substantial shielding to reduce photon exposure. Results of Fig. 8 confirm this reason, where photons traveling along the treatment beam created the majority of the absorbed photon dose in the room floor. Overall, the photon dose value at each point of the floor (as shown in Fig. 9-b) is one order of magnitude greater than the dose received at the opposite point on the ceiling (in Fig. 9-a).

Also, the maximum dose was recorded at a point directly opposite the isocenter on the floor, with a rapid decline in dose distribution surrounding this point, approaching zero within short distances. As depicted in Fig. 9-a, the photon dose at a distance of 50 cm from this point on the floor is nearly negligible. The absorbed photon distribution in Fig. 9-b reveals a pronounced peak at the ceiling point opposite the isocenter, accompanied by a wider distribution around that peak. Notably, a non-zero photon dose is detectable up to approximately 200 cm from the point opposite the isocenter on the ceiling. Moreover, Fig. 9 demonstrates that the incorporation of a polymer shielding layer on the concrete walls significantly reduces the absorbed photon dose both above the ceiling and below the floor. The intensity of dose reduction is more pronounced with the use of different shielding materials (Shield 1, Shield 2, and Shield 3), which contain varying photon attenuator concentrations of lead (30%, 45%, and 60%, respectively). As the thickness of the polymer shield is increased from 1 cm to 2 cm, the efficacy of the dose attenuation becomes increasingly evident.

Third, the absorbed photon dose behind the middle wall of the maze in the treatment room (wall d, as referenced in Figs. 6 and 7), at the points that align vertically

with the isocenter was obtained and shown in Fig. 10. The absorbed photon dose significantly increases as one approaches the edge of the wall d. Figure 6 further confirms the prevalence of photon dose in an ICRU sphere at the edge of wall d, highlighting potential health risks for employees who frequently traverse this area to access the treatment room.

The implementation of the polymer shield demonstrates a notable reduction in photon dose, particularly at the edge of wall d. This reduction is enhanced with the use of Shield 1, Shield 2, and Shield 3 materials, respectively, due to having higher percentages of lead. Furthermore, increasing the thickness of the polymer shield from 1 cm to 2 cm results in more decrease in the absorbed photon dose, underscoring the importance of material selection and shield thickness in radiation protection strategies.

Next, the results of the photon absorbed dose calculations behind the second wall on the right side of the treatment room (designated as (e) in Figs. 6 and 7) are presented in Fig. 11. This investigation indicates that, except for a small area near one edge, photon doses are generally low behind this wall, due to the substantial absorption of photons by the parallel wall located in front (wall d). However, photons that traverse the open space within the maze and subsequently reach the second wall contribute to an increase in the absorbed dose at locations beyond 300 cm (see Fig. 11).

By adding a polymer shield to the wall, although a dose reduction is observed for points before 300 cm, contrarily, at positions near the end of the wall, there is an unexpected increase in the photon absorption dose, which contradicts the radiation protection strategy. This result is intensified for the shielding materials with higher lead percentage and shielding thickness.

The results presented above belong to the Shield 1, Shield 2, and Shield 3 materials. The shielding materials Shield 4, Shield 5, and Shield 6 have similar compositions to Shield 1, Shield 2, and Shield 3, respectively, except that tungsten has been substituted for lead. Since the performance criteria for these three materials are consistent with those previously discussed, repetitive explanations have been avoided.

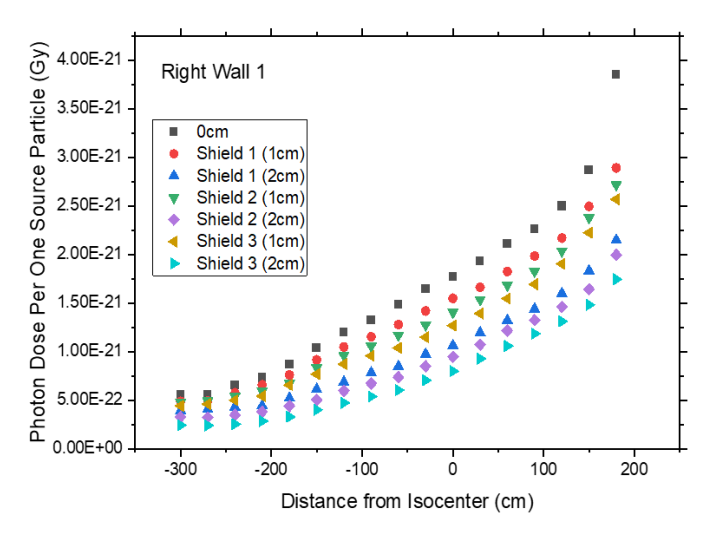


**Figure 10:** Photon absorbed dose behind the middle wall of the maze in the treatment room (wall d in Figs. 5 and 6) with and without the shielding layer of Shield 1, Shield 2 and Shield 3 materials.

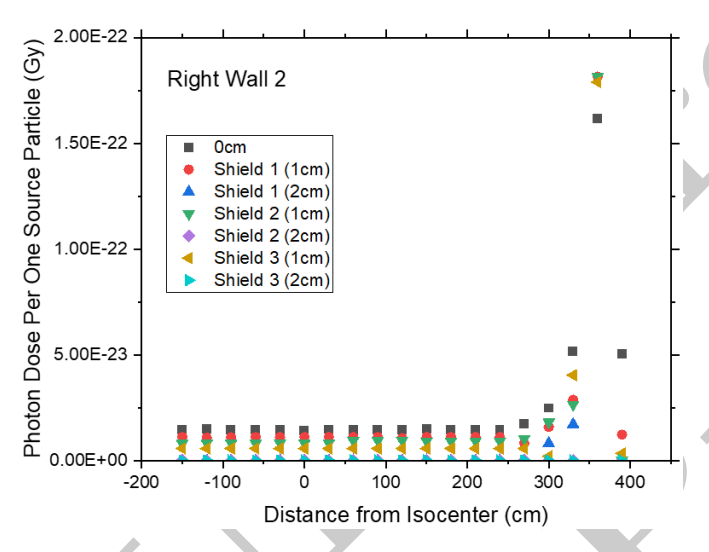


Figure 11: Photon absorbed dose behind the second right wall of the treatment room with and without the shielding layer of Shield 1, Shield 2, and Shield 3 materials.

To assess the impact of lead versus tungsten in the polymer shielding composition, a comparative analysis for Shield 3 and Shield 6 -which contain the highest proportions of their respective elements (60%)- is illustrated in Fig. 12. Figures 12-a, 12-b, and 12-c indicate that while the shielding efficiencies of Shield 3 and Shield 6 are relatively comparable, Shield 6 exhibits superior performance in decreasing photon doses above the treatment room ceiling, below its floor, and behind the wall of the maze (the first wall on the right). This enhanced effectiveness is attributable to the superior photon attenuation properties of tungsten compared to lead.

Figure 12-d confirms that similar to the results illustrated in Fig. 11, there is a negligible photon dose behind the wall (e), particularly near one edge. The findings indicate that a 2 cm thickness of either Shield 3 or Shield 6 significantly reduces the photon dose to zero behind wall (e)

and at distances up to 300 cm. However, at distances exceeding 300 cm, the polymer shielding leads to an increase in the absorbed photon dose compared to an unshielded case, making it unsuitable for wall (e) applications.

## 3.4 Neutron absorbed dose in different locations of treatment room with and without polymer shielding

The isocenter point serves as a reference location in LINAC studies, facilitating comparisons with other investigations. Consequently, this point was selected for the visualization of the photoneutron spectrum. As illustrated in Fig. 13, the spectrum exhibits two distinct peaks. Photoneutrons lose their energies through multiple collisions with the walls, floor and ceiling. It is usually called "roomreturn" or "wall-return" (Vega-Carrillo et al., 2007). The first peak corresponds to these thermal neutrons which reflect into the room. The second peak is associated with fast neutrons, spanning an energy range of 100 keV to 1.5 MeV. It seems these neutrons have no interaction with the walls. Notably, a comparable neutron energy spectrum, consistent with the photoneutron spectrum findings of the current study, has been reported in previous research (Mc-Conn et al., 2011; Abella et al., 2010).

In this section, similar to Section 3.3, we applied a polymeric shielding layer (Summarized in Table 1) to the interior walls, floor, and ceiling of the treatment room. Utilizing the ICRU spheres illustrated in Figures 6 and 7, we calculated the neutron absorbed doses both with and without the polymer shielding on the external walls, above the ceiling, and below the floor of the room. Then, the results were analyzed for the various ingredient percentages and two distinct shielding thicknesses. As in the previous section, we represent the outcomes of shielding materials containing 30%, 45%, and 60% lead, and then, the effect of 60% tungsten is compared to the counterpart material with 60% lead. Relative errors of these calculations are between 6% to 7%.

In Fig. 14, the neutron dose is depicted in two directions (i.e., x and y axes) perpendicular to the treatment beam. Unlike the photon dose curves, which exhibit sharp peaks at the isocenter and a sudden drop around this point (as shown in Fig. 7), the neutron dose in these two directions centered around the isocenter has a broad peak, with gradual decreases at both sides. This difference arises from the fact that neutrons are produced unintentionally and non-targetedly within the treatment room, and as a result, they are distributed throughout almost the entire space of the room. The broad peak of the neutron dose around the isocenter is due to the higher intensity of treatment photons in the direction of the main beam (i.e., towards the isocenter) and its close proximity. Thus, the probability of  $(\gamma, n)$  in the vicinity of the treatment beam increases.

The neutron dose in Fig. 14 shows a greater decrease for the shielding materials Shield 1, Shield 2, and Shield 3, respectively. Among these three materials and the two thicknesses examined, Shield 1 with a thickness of 2 cm results in the greatest reduction in neutron dose. It appears that Shield 2 and Shield 3 materials, with a higher per-

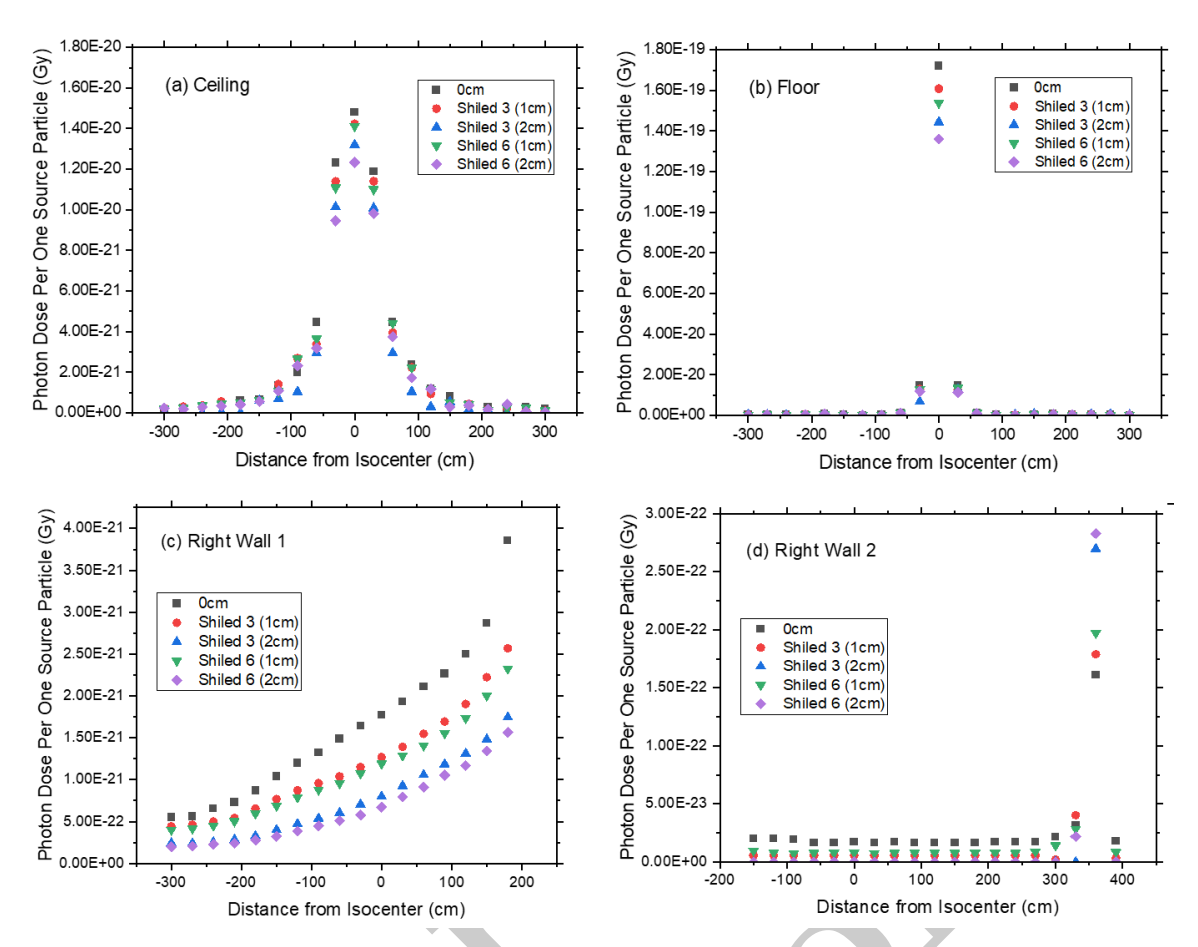


Figure 12: Photon absorbed dose (a) above the ceiling and (b) below the floor of the treatment room, (c) behind the middle wall of the maze (The first wall on the right), and (d) behind the second wall on the right of the treatment room; with and without the shielding layer of Shield 3 and Shield 6 materials.

centage of lead, increase the probability of photonuclear interactions within the shielding, and then, some produced neutrons enter the treatment room and increase the neutron flux inside the room.

Figure 15 represents the results of the neutron dose calculations above the ceiling of the treatment room comparing scenarios with and without adding a layer of Shield 1, Shield 2, and Shield 3 materials. The data reveal that the neutron dose peaks at a location opposite the center of the ceiling and gradually diminishes in surrounding areas. Notably, as the percentage of photon attenuators -such as lead or tungsten- within the polymer shielding composition increases, the overall height of the neutron dose curve decreases. This trend indicates that higher concentrations of lead or tungsten, combined with a specific percentage of boron carbide (7.5% in this study), effectively enhance photon attenuation and boost neutron absorption. When Shield 3, with a thickness of 2 cm, is employed, the neutron dose distribution exhibits the most significant reduction at its peak, and at further distances approaches zero.

Regarding the neutron dose beneath the floor, the results show nearly negligible neutron doses. It can be concluded that the concrete thickness of the floor which is 20 cm thicker than the ceiling absorbs the majority of neutrons. Therefore, these results were not plotted. Figure 16 indicates the neutron-absorbed dose behind the mid-

dle wall of the maze (wall d) in the treatment room, both with and without the incorporation of a shielding layer. It can be seen that the neutron absorbed dose increases and reaches a maximum with a sudden increase at the edge of the corridor. It is similar to the photon dose results behind this wall in Fig. 10.

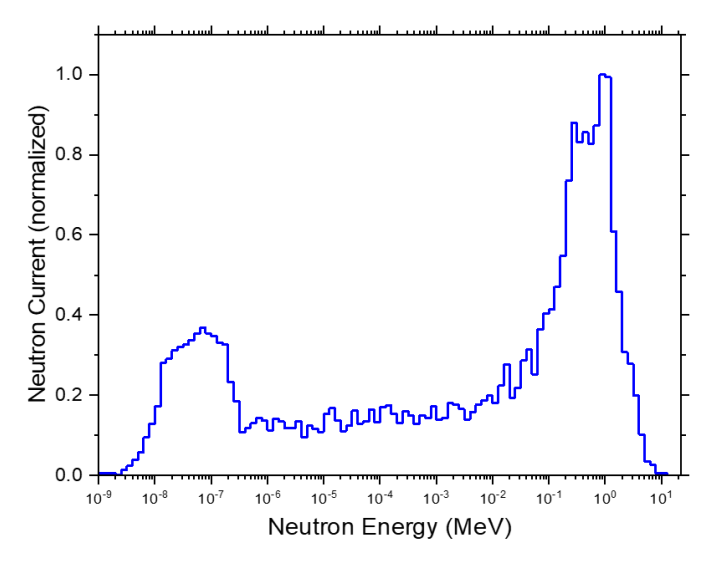


**Figure 13:** Neutron energy spectrum produced by an 18 MV LINAC at isocenter.

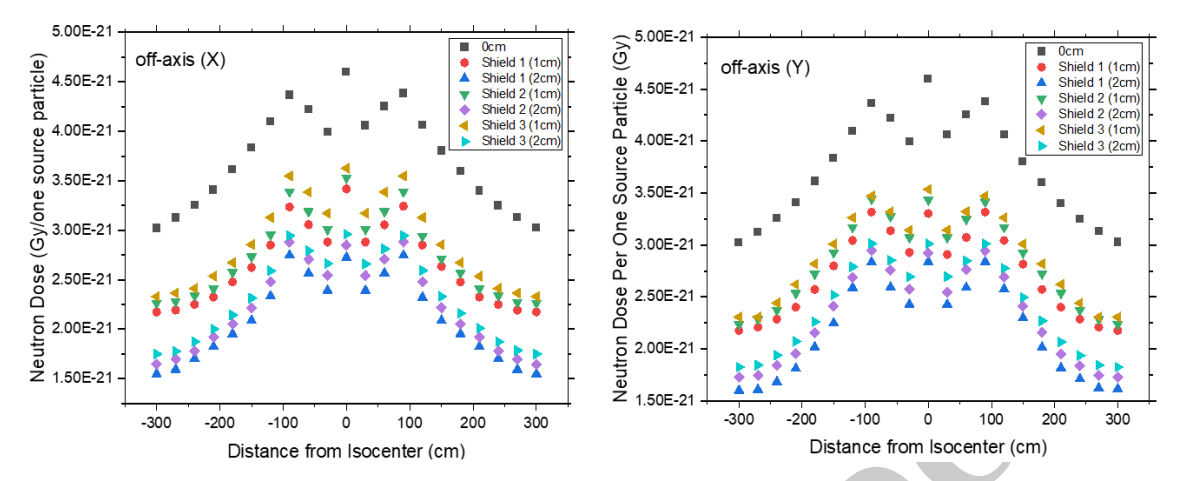


Figure 14: Neutron dose in the x and y directions perpendicular to the treatment beam, with and without a shielding layer of Shield 1, Shield 2 and Shield 3 materials.

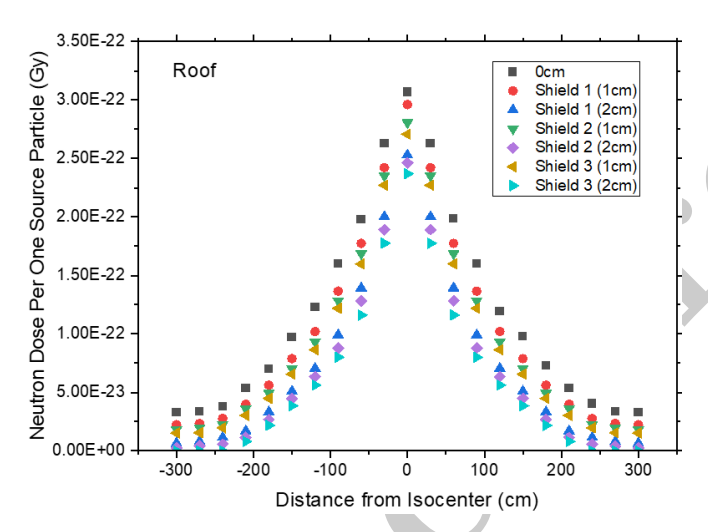


Figure 15: Neutron absorbed dose outside the treatment room above its ceiling with and without the shielding layer of Shield 1, Shield 2, and Shield 3 materials.

The neutron energy deposition shown in Fig. 7 also confirms the dominant neutron dose in a sphere on the last points (last sphere) of wall d. In general, the integration of a polymer shielding layer into the concrete walls reduces the neutron dose significantly. If the percentage of lead in the polymer shield increases, it has a positive effect on reducing the neutron dose. This is attributed to the fact that neutrons interacting with the wall generally lose energy through multiple successive collisions, and subsequently are absorbed as they traverse the polymer shielding layer and the concrete substrate. Among the materials tested, Shield 3, with a thickness of 2 cm, demonstrates the highest neutron absorption capacity, thereby achieving the most substantial reduction in the neutron dose.

The results obtained for the neutron dose with the presence of three additional shielding materials, Shield 4, Shield 5 and Shield 6 are respectively similar to those obtained for Shield 1, Shield 2, and Shield 3, as shown in Figs. 14 to 16. Therefore, we have avoided repeating similar content. However, to investigate the effect of lead and tungsten on the neutron dose at various points in the treatment room, we have compared some of the results

obtained for Shield 3 to Shield 6, which contain 60% lead and 60% tungsten, respectively.

Figure 17 shows a similar trend for the two shielding materials, Shield 3 and Shield 6, in reducing neutron dose at different places inside and outside the treatment room.

The results indicate that both materials effectively reduce the neutron dose compared to the unshielded condition. Notably, Shield 6 demonstrates a more significant reduction in neutron dose, attributable to its 60% tungsten composition, which enhances photon attenuation. Adeli et al. (Adeli et al., 2016) in their study, also found that the composite shielding reinforced with tungsten oxide exhibits a higher mass attenuation coefficient compared to that reinforced with lead oxide. Our results showed that polymer shielding also reduces neutron dose above the ceiling and beneath the floor.

The absorbed neutron dose calculations for the floor and the area behind the second wall on the right side of the treatment room are not included, as the concrete shield effectively absorbs neutrons in these regions. Consequently, the neutron dose in the area beneath the floor and behind the wall approaches zero.

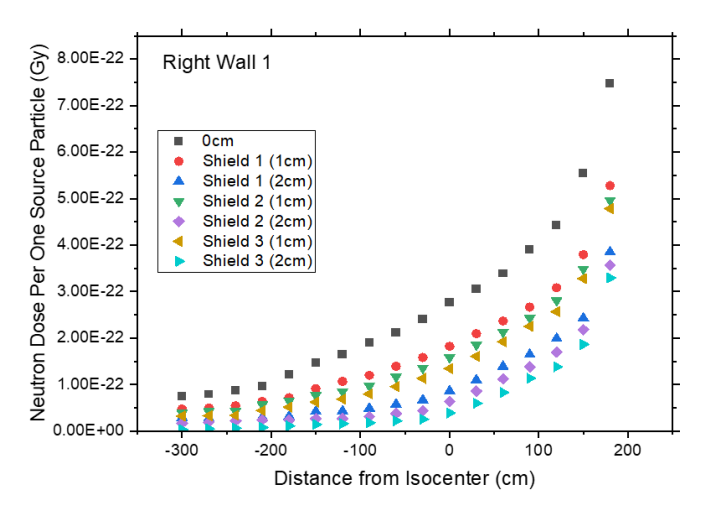


**Figure 16:** Neutron absorbed dose behind the middle wall of the maze (wall d) in the treatment room, with and without the shielding layer of Shield 1, Shield 2 and Shield 3 materials.

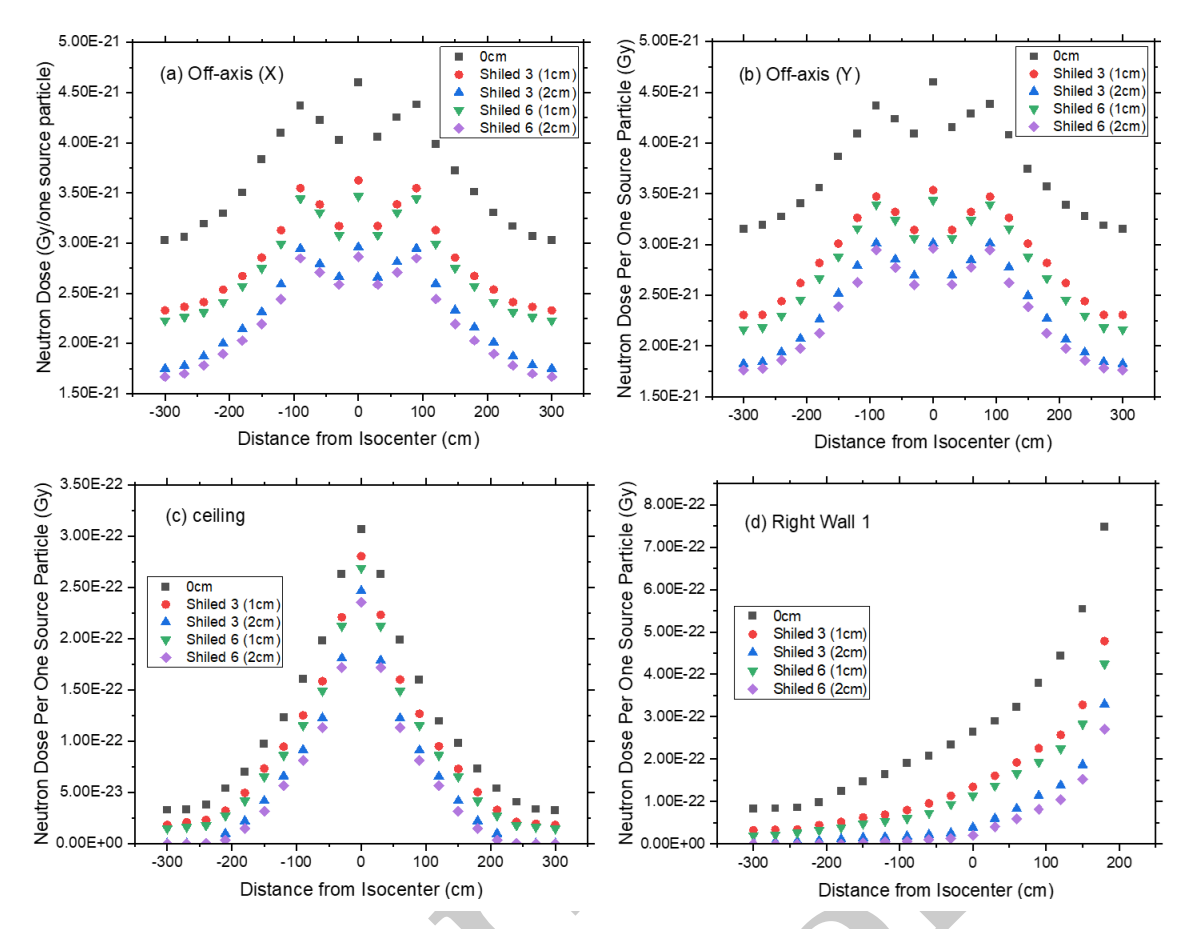


Figure 17: Neutron absorbed dose (a) perpendicular to the beam in the x direction, (b) perpendicular to the beam in the y direction, (c) above the ceiling, and (d) behind the middle wall of the maze (i.e., the first wall on the right); with and without the shielding layer of Shield 3 and Shield 6 materials.

# 3.5 Comparison of polymeric shielding material results to the pure lead, in reducing photon absorbed dose

To make the results of the shielding material under investigation more sensible, we calculated the absorbed photon dose by considering a pure lead layer to the concrete of the walls, ceiling, and floor. Subsequently, the point on each wall exhibiting the highest photon absorbed dose was identified. The photon absorbed dose value within a sphere positioned at this location on the wall was compared between the polymer and the pure lead shields. This comparison was conducted separately for the direction perpendicular to the treatment beam at the isocenter, as well as for the first and second right walls, ceiling, and floor of the treatment room.

As previously indicated, the maximum absorbed photon dose occurs at the isocenter, which is situated at the center of the xy plane perpendicular to the treatment beam and highlighted in red within the sphere depicted in Fig. 18-a. The addition of either a polymer or pure lead shielding layer to the concrete walls of the treatment room does not significantly reduce the photon dose at the isocenter, as supported by the findings illustrated in Fig. 8. In Fig. 18-b, the effect of shielding layers applied to the concrete wall d (i.e., the first right wall of the maze) was compared to adding pure lead. Notably, at the point

marked in red on this wall, the 1 cm thick layer of pure lead shielding does not yield a reduction in the absorbed dose, whereas the polymer shielding layer demonstrates a more effective attenuation. This discrepancy can be attributed to the ability of polymer shielding to absorb neutrons, thereby mitigating the production of secondary photons resulting from  $(n,\gamma)$  interactions of neutrons that traverse the concrete wall and interact with materials at the edge of this wall. In contrast, pure lead shielding exhibits a higher probability of neutron interaction, leading to increased photon production.

The maximum absorbed photon dose is recorded at locations above the ceiling and below the floor of the treatment room, specifically at points directly opposite the isocenter on both the ceiling and floor. Figures 18-c and 18-d illustrate the comparative effectiveness of a polymer shielding layer versus a pure lead layer in reducing the absorbed dose at these critical points. The areas of interest are highlighted in red in the corresponding images. The most significant dose reduction is achieved with Shield 6, which is composed of 60% tungsten, followed closely by Shield 3, which contains 60% lead. In contrast, Shields 1, 2, 4, and 5, which incorporate lower proportions of lead or tungsten, demonstrate a lower shielding efficiency in decreasing the photon dose. Overall, it can be concluded the 2 cm thickness of Shield 6 is equivalent to that of a 3 mm layer of pure lead in photon dose reduction.

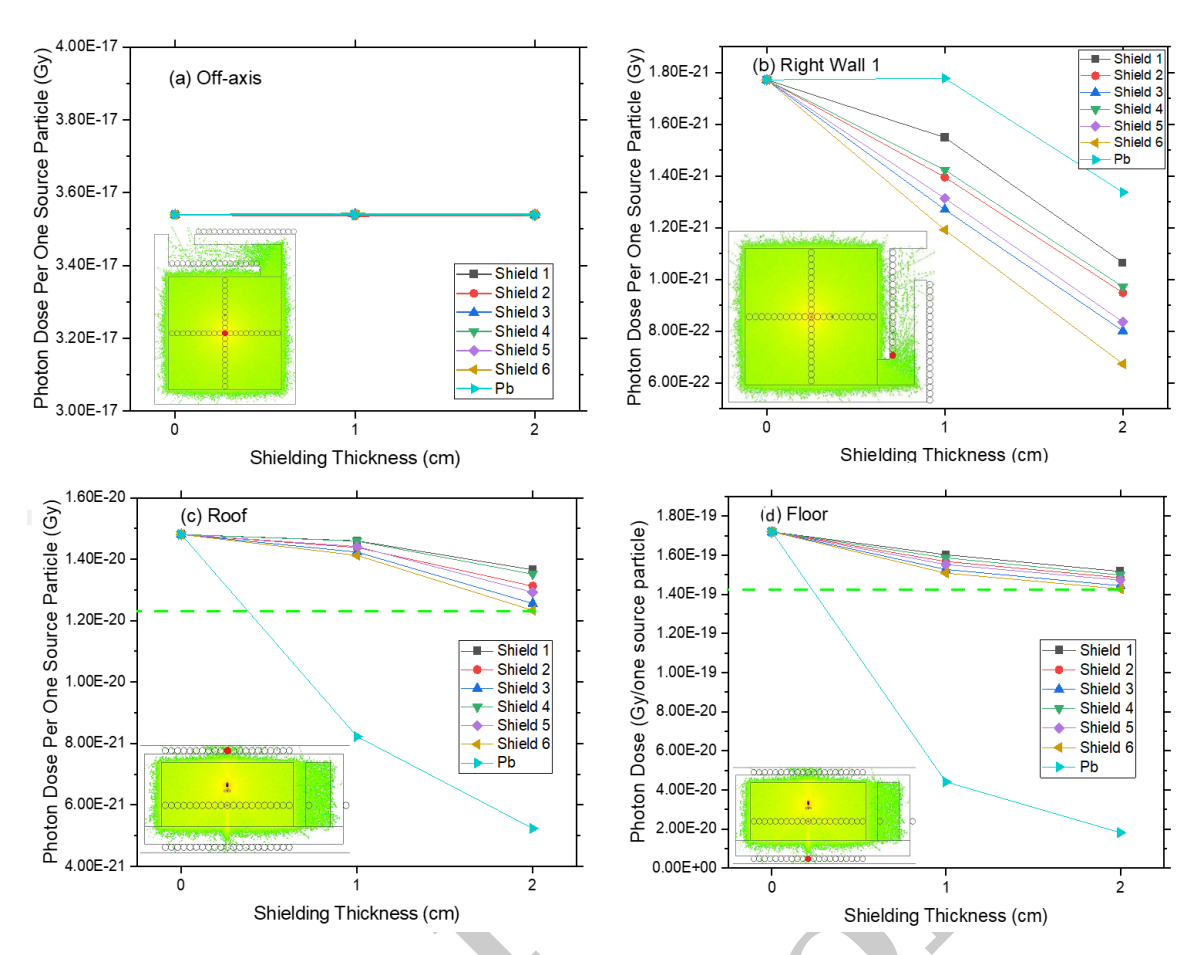


Figure 18: Comparison of the effect of polymeric and pure lead shielding layers on treatment room walls on absorbed photon dose, (a) at the isocenter point, (b) at the edge of the first wall on the right, (c) at a point opposite the isocenter above the room ceiling, and (d) at a point opposite the isocenter below the room floor.

#### 3.6 Neutron Dose rate in maze

To investigate the streaming in the maze of the LINAC room, we considered 5 point detectors (shown in Fig. 7 by red pluses). Then, the dose rate at these points was calculated by USRBIN card (in units of pSv). The results were normalized to provide 1 Gy of photon absorbed dose in the isocenter. When polymer-based shielding was not added, the neutron dose rate decreased by a factor of 8.32 from point 1 to 5 (they are 4.5 m apart), along the maze, which. This result is in agreement with the results of Rebello et al. (Rebello et al., 2010) who simulated the same LINAC model, electron beam energy and geometry using MCNPX. They obtained in the maze of the LINAC room, between two points apart from each other 4.4 m, the dose rate of neutrons decreases by a factor of 7.68. In both studies the first point was located at the edge of the maze and the last one was near the end of the corridor in the maze.

These results are more realistic when they are compared with the allowed annual dose. Assuming a daily dose of 70 Gy is prescribed to treat a type of cancer, the neutron dose rate at the edge of the maze is  $3.59~\mathrm{mSv}$  and  $1.30~\mathrm{mSv}$  without and with the polymeric shield. It is notable that to obtain the dose rate values (mSv.h<sup>-1</sup>), one has to know the current of the LINAC machine.

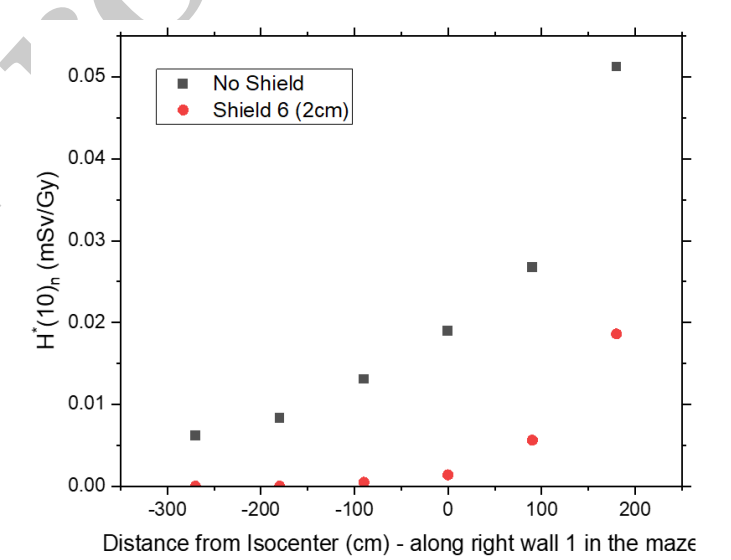


Figure 19: Dose rate of neutrons in the maze of LINAC room with and without using polymer-based shielding on the concrete wall.

#### 4 Conclusions

In this research, using FLUKA code (Version 2011.2c.6), the components of the head of a C/D2300 linear accelerator manufactured by Varian (18 MeV) were simulated in

Location	Percentage of decrease or increase in photon dose	Percentage of decrease or increase in neutron dose
Isocenter on the xy plane	0	-35
Opposite the isocenter above the roof	-17	-22
Opposite the isocenter under the floor	-17	In this location, the dose without polymer shielding is almost zero
Edge of the maze in the first right wall	-60	-60
Near the end edge of the second right wall	+45	In this location, the dose without polymer shielding is almost zero

**Table 3:** Effect of using Shield 6 material with a thickness of 2 cm on the absorbed photon and neutron dose in some parts of the radiotherapy room.

actual sizes in a radiotherapy room. Since the objective of this research is to investigate the addition of a polymer shielding layer on the concrete walls of the treatment room equipped with a linear accelerator, performing calculations from the electron beam to the walls of the treatment room is highly time-consuming and requires transporting billions of electrons.

As an innovation in the present study, instead of using an electron source and transporting particles started from the source in each calculation in the FLUKA code, similar to the SSW card in MCNP, an alternative photon source (with an energy spectrum dependent on the emission direction, exhibiting similar behavior to an integrated simulation) was utilized in the calculations. This source not only saves execution time and reduces computational uncertainty, but also generates phase space around the target.

Another notable innovation of this research is the design of a multilayer shield for the walls of treatment rooms. Multilayer shields can be utilized in situations where the thickness of the concrete layer in the room is insufficient or when the treatment room equipment or accelerator devices have been upgraded and require more appropriate shielding. The shield proposed in the present research reduces the necessary thickness of the material due to the presence of photon and neutron attenuators within a polymeric matrix. Therefore, it is practical in locations where space is limited. In addition to reducing volume, this shield is lightweight and flexible due to its polymeric base. Thus, instead of incurring heavy costs and long durations for major renovations of the treatment room structure, the proposed shielding layer can be easily added to the treatment room without damaging the existing walls. Furthermore, in the design and construction of new treatment rooms, particularly in spaces with limited area, this shield can reduce the necessary thickness of concrete and can serve as an overlay on concrete due to its photon and neutron attenuators within a polymeric matrix. Additionally, an optimal thickness of this shield can convert a non-radiation room into a treatment room equipped with a medical accelerator. Due to its non-toxicity and flexibility, it can also be used as shielding in radiography and CT scan departments.

In order to investigate multilayer shielding for the LINAC room, the next step involved adding a polymer shielding layer to the interior part of the concrete walls, floor, and ceiling of the treatment room. The absorbed

doses of photons and neutrons were measured outside the walls, above the ceiling, and below the floor of the room; with and without considering this shielding. Subsequently, the results obtained from different percentages of the constituent materials and two different thicknesses of the shield were compared.

The results of this study indicated that adding a polymer shielding layer on the concrete walls of the treatment room does not affect the reduction of photon dose at a plane (x-y) perpendicular to the treatment beam, centered at the isocenter. In contrast to the photon dose, neutron dose decreases significantly in this plane, especially at the isocenter. Therefore, a thickness of 2cm Shield 1 material yields the greatest reduction in neutron dose. As with adding a polymer shielding layer to the concrete ceiling and floor, it can reduce the absorbed photon dose outside the room as expected. This reduction effect is more pronounced for the Shield 6 (containing 60% tungsten) at a thickness of 2 cm compared to other materials studied, even containing 60% lead.

Investigation of photon and neutron doses behind and along the first right concrete wall (wall d) in the treatment room, exhibits an increasing trend in photon dose, reaching its maximum value at the edge of this wall with a sudden increase. When considering a polymer shielding layer on this wall, a significant reduction in the photon dose is observed, especially as one approaches the edge of the wall (d). Additionally, the sudden increase in dose at the edge of the wall is eliminated. Generally, the Shield 6 material with a thickness of 2 cm, shows the greatest reduction among the materials examined. An evaluation of the neutron dose behind this wall also confirms this finding. But about the second right wall (wall e in Figs. 6 and 7), the application of a polymer shielding layer, at the beginning of the wall (along it) reduces the photon dose but then results in a sharp increase at the end of the wall. Therefore, the use of polymer shielding for this wall is not recommended. The neutron dose behind this wall with no shield is almost zero.

The comparison of the results obtained from the polymer shield with those from pure lead indicates that a polymer shield of 2 cm thickness made of Shield 6 material is equivalent to approximately 3 mm thickness of pure lead. In general, the use of a polymer shielding layer made from Shield 6 material on the inner layer of the concrete ceiling, floor, and walls of the treatment room is recommended, except for the second wall on the right side (wall e in Figs.

5 and 6). Table 3 summarizes the effect of using 6 Shield materials at a thickness of 2cm on photon and neutron doses.

The optimal thickness required depends on the specifications of the accelerator, its energy, the dimensions of the treatment room, and the thickness of the concrete wall shielding, which can be calculated based on these specifications.

#### Conflict of Interest

The authors declare no potential conflict of interest regarding the publication of this work.

#### References

Abdul Haneefa, K., Cyriac, T. S., Musthafa, M., et al. (2014). FLUKA Monte Carlo for basic dosimetric studies of dual energy medical linear accelerator. *Journal of Radiotherapy*, 2014(1):343979.

Abella, V., Miro, R., Juste, B., et al. (2010). Monte Carlo model of the female RANDO phantom irradiation with an Elekta Precise linear accelerator. Nuclear Instruments and Methods in Physics Research Section A: Accelerators, Spectrometers, Detectors and Associated Equipment, 619(1-3):230–233.

Adeli, R., Shirmardi, S. P., and Ahmadi, S. J. (2016). Neutron irradiation tests on  $B_4C/epoxy$  composite for neutron shielding application and the parameters assay. *Radiation Physics and Chemistry*, 127:140–146.

Ali, K. M., Mohammad, K. K., and Atallah, F. S. (2018). Calculation of radiation doses using shields for nanoparticles tungsten oxide WO<sub>3</sub> mixed with epoxy. *J. Radiat. Nucl. Appl*, 3:191-197.

Asgari, M., Afarideh, H., Ghafoorifard, H., et al. (2021). Effects of particle size and weight percentage of heavy metal elements on photon shielding efficiency of reinforced polymer composites. *International Journal of Radiation Research*, 19(1):55–61.

Ashoor, M., Khorshidi, A., and Sarkhosh, L. (2019). Introducing a novel coefficient on mixed-nanoparticles material: relationship between the theoretical and experimental densities. *Heliyon*, 5(7).

Auditore, L., Barna, R., de Pasquale, D., et al. (2005). A compact 5 MeV S-band electron linac based x-ray source for industrial radiography. In *Proceedings of the 2005 Particle Accelerator Conference*, pages 2428–2430. IEEE.

Brkić, H., Kasabašić, M., Ivković, A., et al. (2018). Influence of head cover on the neutron dose equivalent in monte carlo simulations of high energy medical linear accelerator. *Nuclear Technology & Radiation Protection*, 33(2):217–222.

Dawn, S., Pal, R., Bakshi, A., et al. (2018). Evaluation of in-field neutron production for medical LINACs with and without flattening filter for various beam parameters-Experiment and Monte Carlo simulation. *Radiation Measurements*, 118:98–107.

Edwards, C. and Mountford, P. (2004). Near surface photon energy spectra outside a 6 MV field edge. *Physics in Medicine & Biology*, 49(18):N293.

El-Nahal, M. A., Elsafi, M., Sayyed, M., et al. (2021). Understanding the effect of introducing micro-and nanoparticle bismuth oxide ( $\mathrm{Bi}_2\mathrm{O}_3$ ) on the gamma ray shielding performance of novel concrete. *Materials*, 14(21):6487.

Ferrari, A., Ranft, J., Sala, P. R., et al. (2005). FLUKA: A multi-particle transport code (Program version 2005). Number CERN-2005-10. Cern.

Funk, R. K., Stockham, A. L., and Laack, N. N. I. (2016). Basics of radiation therapy. *Clinical cardio-oncology. Amsterdam: Elsevier*, pages 39–60.

Ghasemi-Jangjoo, A. and Ghiasi, H. (2019). MC safe bunker designing for an 18 MV linac with nanoparticles included primary barriers and effect of the nanoparticles on the shielding aspects. *Reports of Practical Oncology and Radiotherapy*, 24(4):363–368.

Goorley, T., James, M., Booth, T., et al. (2012). Initial MCNP6 release overview. *Nuclear Technology*, 180(3):298–315.

Hassan, Z. E.-T., Farag, N. M., and Elshemey, W. M. (2018). A versatile program for the calculation of linear accelerator room shielding. *Journal of Radiological Protection*, 38(2):666.

Hernandez-Adame, L., Contreras-Sandoval, H., Vega-Carrillo, H. R., et al. (2011). Design of a treatment room for an 18-MV linac. *Nuclear Technology*, 175(1):105–112.

Horst, F., Czarnecki, D., and Zink, K. (2015). The influence of neutron contamination on dosimetry in external photon beam radiotherapy. *Medical Physics*, 42(11):6529–6536.

Howell, R. M., Kry, S. F., Burgett, E., et al. (2009). Secondary neutron spectra from modern Varian, Siemens, and Elekta linacs with multileaf collimators. *Medical Physics*, 36(9Part1):4027–4038.

Jabbari, N. and Hashemi-Malayeri, B. (2009). Monte Carlo modeling of electron beams from a NEPTUN 10PC medical linear accelerator. *Nukleonika*, 54:233–238.

Kosako, K., Oishi, K., Nakamura, T., et al. (2014). Optimum shielding structure for the wall of medical linac facility. *Progress in Nuclear Science and Technology*, 4:276–279.

Ma, A., Awotwi-Pratt, J., Alghamdi, A., et al. (2008). Monte Carlo study of photoneutron production in the Varian Clinac 2100C linac. *Journal of Radioanalytical and Nuclear Chemistry*, 276:119–123.

Martinez-Ovalle, S., Barquero, R., Gomez-Ros, J., et al. (2011). Neutron dose equivalent and neutron spectra in tissue for clinical linacs operating at 15, 18 and 20 MV. *Radiation Protection Dosimetry*, 147(4):498–511.

McConn, R. J., Gesh, C. J., Pagh, R. T., et al. (2011). Compendium of material composition data for radiation transport modeling. Technical report, Pacific Northwest National Lab.(PNNL), Richland, WA (United States).

Morgan, H., Wu, R., and Reber, E. (2006). Radiation protection in the design of radiotherapy facilities. International Atomic Energy Agency.

Patil, B., Chavan, S., Pethe, S., et al. (2011). Estimation of neutron production from accelerator head assembly of 15 MV medical LINAC using FLUKA simulations. *Nuclear Instruments and Methods in Physics Research Section B: Beam Interactions with Materials and Atoms*, 269(24):3261–3265.

Razghandi, S., Karimi-Shahri, K., and Firoozabadi, M. (2021). Evaluation of neutron spectra and dose equivalent from a Varian 2100C/D Medical Linear Accelerator: Monte Carlo simulation. Radioprotection, 56(2):93-101.

Rebello, W., Silva, A., Facure, A., et al. (2010). Monte Carlo simulation of photoneutrons streaming inside radiotherapy treatment rooms as a function of gantry angles. *Progress in Nuclear Energy*, 52(3):278–281.

Rosenberg, I. (2008). Radiation oncology physics: a hand-book for teachers and students. *British Journal of Cancer*, 98(5):1020–1020.

Salimi, M., Ghal-Eh, N., and Amirabadi, E. A. (2018). Characterization of a new shielding rubber for use in neutron–gamma mixed fields. *Nuclear Science and Techniques*, 29:1–8.

Soltani, Z., Beigzadeh, A., Ziaie, F., et al. (2016). Effect of particle size and percentages of boron carbide on the thermal neutron radiation shielding properties of HDPE/B<sub>4</sub>C composite: Experimental and simulation studies. *Radiation Physics and Chemistry*, 127:182–187.

Soppera, N., Dupont, E., Bossant, M., et al. (2017). JANIS Book.

Tekin, H. O., Singh, V. P., and Manici, T. (2017). Effects of micro-sized and nano-sized WO<sub>3</sub> on mass attenuation coeffi-

cients of concrete by using MCNPX code. Applied Radiation and Isotopes, 121:122–125.

Toossi, M. T. B., Behmadi, M., Ghorbani, M., et al. (2013). A Monte Carlo study on electron and neutron contamination caused by the presence of hip prosthesis in photon mode of a 15 MV Siemens PRIMUS linac. *Journal of Applied Clinical Medical Physics*, 14(5):52–67.

Uddin, M. F., Akter, S., Ahmed, M., et al. (2024). Photoneutron production mechanisms, their characteristics, and shielding strategies in high-energy linac environment: A review. *Journal of Radiation Research and Applied Sciences*, 17(3):101031.

Vega-Carrillo, H., Martinez-Ovalle, S., Lallena, A., et al. (2012). Neutron and photon spectra in LINACs. *Applied Radiation and Isotopes*, 71:75-80.

Vega-Carrillo, H. R., Manzanares-Acuña, E., Iñiguez, M. P., et al. (2007). Study of room-return neutrons. *Radiation Measurements*, 42(3):413–419.

Verdipoor, K. and Mesbahi, A. (2020). Radiation shielding features of ordinary and high-density concretes loaded with PbO micro and nanoparticles against high-energy photons. *Iranian Journal of Medical Physics*, 17(3):205–212.

Wang, J., Trovati, S., Borchard, P. M., et al. (2017). Thermal limits on MV x-ray production by bremsstrahlung targets in the context of novel linear accelerators. *Medical Physics*, 44(12):6610–6620.

Wille, K. (2000). The physics of particle accelerators: an introduction. Clarendon Press.

©2025 by the journal.

RPE is licensed under a Creative Commons Attribution-NonCommercial 4.0 International License (CC BY-NC 4.0).





#### To cite this article:

E. Asadi Amirabadi, M.R. Pahlavani, N. Ghal-Eh (2025). Impact of polymer shielding layer on absorbed dose distribution in an 18 MeV LINAC treatment room: A FLUKA simulation study. *Radiation Physics and Engineering*, In Press.

DOI:

To link to this article: